Journal of
Microscopy

Journal of Microscopy, Vol. 245, Pt 1 2012, pp. 63–71
Received 4 July 2011, accepted 3 August 2011

doi: 10.1111/j.1365-2818.2011.03544.x

Effects of aberrations and specimen structure in conventional, confocal and two-photon fluorescence microscopy

R.D. SIMMONDS, T. WILSON & M.J. BOOTH
Department of Engineering Science, University of Oxford, Parks Road, Oxford, UK

Key words. Aberrations, confocal microscope, fluorescence, specimen structure, two-photon.

Summary

Specimen-induced aberrations cause a reduction in signal levels and resolution in fluorescence microscopy. Aberrations also affect the image contrast achieved by these microscopes. We model the effects of aberrations on the fluorescence signals acquired from different specimen structures, such as point-like, linear, planar and volume structures, when imaged by conventional, confocal and two-photon microscopes. From this we derive the image contrast obtained when observing combinations of such structures. We show that the effect of aberrations on the visibility of fine features depends upon the specimen morphology and that the contrast is less significantly affected in microscopes exhibiting optical sectioning. For example, we show that point objects become indistinguishable from background fluorescence in the presence of aberrations, particularly when imaged in a conventional fluorescence microscope. This demonstrates the significant advantage of using confocal or two-photon microscopes over conventional instruments when aberrations are present.

Introduction

It is widely acknowledged that specimen-induced aberrations detrimentally affect the quality of the image, which can be achieved by high-resolution optical microscopes (Gibson and Lanni, 1992; Hell et al., 1993; Booth et al., 1998). These aberrations limit the ability of microscopes to image deep within thick specimens (Diaspro et al., 2002), although recent developments in adaptive optics for aberration correction have led to improvements (Booth, 2007; Girkin et al., 2009; Ji et al., 2010). The effects of aberrations on microscope images include reduction in resolution, blurring and reduction of intensity. An important but less well-known consequence of specimen-induced aberrations is that they affect different specimen features in different ways (Débarre et al., 2009). It is important to appreciate these differences because they have implications on the visibility and contrast with which specimen structures appear in the final image.

In this paper, we model the imaging of idealized specimen structures (point, line, plane and volume objects) in conventional, confocal and two-photon fluorescence microscopes. We examine the effects of aberrations on the peak image intensity for each of these structures and show that the sensitivity to aberrations is highest for lower dimensional objects. The effects of aberrations on image contrast are also considered when different structures are present in the same specimen, for example when a point-like object is embedded in a fluorescent volume. As aberrations affect differently the peak image intensity for each specimen structure, we show that there is a differential effect on the image contrast for combinations of structures. This leads to the possibility that small objects may be in effect invisible, whilst an appreciable background fluorescence is detected. This phenomenon could have important consequences in the interpretation of images in biological microscopy, where it may not be obvious that the apparent absence of small features is due to aberrations.

Correspondence to: Martin Booth, Department of Engineering Science, University of Oxford, Parks Road, Oxford OX1 3PJ, UK. E-mail: martin.booth@eng.ox.ac.uk.

Aberrations and the pupil function

For the analysis in this paper, we assume that the aberrations are phase-only in nature and can be represented by phase variation introduced into the pupil of the objective lens. For convenience, we assume that this pupil has a normalized radius of one. The complex pupil function is thus given by

$$P(r,\theta) = \exp[j\phi(r,\theta)]\ r \leq 1, 0 \text{ otherwise} \qquad (1)$$

where $\phi(r,\ \theta)$ is the phase aberration and j is the imaginary unit. We model the aberration as a series of Zernike polynomials, which are represented by the functions $Z_i(r,\theta)$:

$$\phi(r,\theta) = \sum a_i Z_i(r,\theta), \qquad (2)$$

where a_i represents the coefficient of each mode, measured in radians. The definition of the Zernike polynomials is explained in the Appendix. We do not include the low-order polynomials

piston, tip, tilt and defocus in our analysis as they do not contribute to a change in the image quality (although tip, tilt and defocus do cause image distortion; Schwertner et al., 2007).

In the analysis that follows, we consider the effects on image quality of single Zernike modes and of random combinations of multiple Zernike modes. In the case of single modes, the phase aberration $\phi(r, \theta) = a_i Z_i(r, \theta)$. The effects are illustrated using the six Zernike modes 5–10, encompassing the lowest order astigmatism, coma and trefoil modes. Although results from other modes could have been presented, the trends shown for the first six Zernike modes are found to be common to all other Zernike modes and hence for brevity we present results only for the first six in detail. However, we include higher order modes, such as spherical, in the analysis of random aberrations. For these further calculations, we used random combinations of a set of N Zernike modes, for which the phase was defined as

$$\phi(r, \theta) = A \sum_{i=1}^{N} a_i Z_i(r, \theta), \tag{3}$$

where A is the aberration amplitude. To generate the random aberration, the modal coefficients a_i were assigned a random value between 0 and 1. The coefficients were then renormalized so that the total mean square value $\sum_i a_i^2$ was 1. This ensured that the rms amplitude of the phase defined by Eq. (3) was equal to A.

For calculations involving volume structures it was necessary to calculate the field in out-of-focus planes. For this purpose, an additional quadratic phase component is included in the pupil function:

$$P(r, \theta) = \exp\left[j\phi(r, \theta) + j\frac{ur^2}{2} \right], \tag{4}$$

where u is the normalized axial coordinate, related to the real coordinate z by

$$u = \frac{8\pi z}{\lambda} \sin^2\left(\frac{\alpha}{2}\right), \tag{5}$$

where λ is the wavelength and α is the aperture angle of the objective lens (Gu, 1996).

Image formation in fluorescence microscopes

For all incoherent fluorescence microscopes, the image intensity can be described by the convolution of the intensity point spread function (IPSF) of the imaging lens evaluated at the fluorescence wavelength, H, with the fluorescence distribution, f (Wilson and Sheppard, 1984):

$$I = H * f, \tag{6}$$

where $*$ denotes the convolution operation. In the case of the conventional, non-scanning fluorescence microscope, the IPSF H_{conv} is mathematically equivalent to the modulus squared of the amplitude point-spread function (PSF) h and can be written as

$$H_{\text{conv}} = |h|^2, \tag{7}$$

whereas for the confocal microscope, the effective IPSF H_{conf} is given by the product of the IPSF of the objective lens which excites the fluorescence and that of the objective which focuses the fluorescence onto the confocal pinhole. If we ignore the Stokes shift between the excitation and the fluorescence and assume that the illumination and detection objectives are the same, then the effective IPSF is given by (Wilson and Sheppard, 1984):

$$H_{\text{conf}} = |h|^4. \tag{8}$$

Using the scalar approximation to diffraction theory, the field in the focus of the objective lens can be expressed as the Fourier transform of the pupil function. Hence, the amplitude PSF h is given in two dimensions by

$$h(t, w) = \int_{r=0}^{1} \int_{\theta=0}^{2\pi} P(r, \theta) \exp[j(tr\cos\theta + wr\sin\theta)] r\,\mathrm{d}r\,\mathrm{d}\theta, \tag{9}$$

where $(t, w) = (\frac{2\pi x NA}{\lambda}, \frac{2\pi y NA}{\lambda})$, x and y are Cartesian coordinates in the image plane and NA is the numerical aperture of the objective lens. Because $P(r, \theta)$ incorporates aberrations (Eq. 1), Eq. (9) may be used to calculate the aberrated amplitude PSF. In Eq. (9) and from this point on we have omitted pre-multiplying constants to the integrals, because the constants have no effect on the normalized results that are presented.

The two-photon excitation efficiency is proportional to the square of the intensity of the excitation light and so can be described by the IPSF in Eq. (8) evaluated at the excitation wavelength. This is the same expression as that used to describe the confocal microscope, so the effects of aberrations on both types of microscope can be modelled by the same equations.

The image formation process described by Eq. (6) can equivalently be written in terms of the product of the optical transfer function, C, and the Fourier transform of the fluorescence distribution, F (Wilson and Sheppard, 1984), written here in two dimensions:

$$I(t, w) = \iint C(m, n) F(m, n) \exp[-j(tm + wn)]\,\mathrm{d}m\,\mathrm{d}n, \tag{10}$$

where C is the Fourier transform of H, F is the Fourier transform of f and (m, n) are the normalized spatial frequencies in the Fourier domain. In the case of the conventional, non-scanning fluorescence microscope, C can be defined as

$$C_{\text{conv}}(m, n) = P(m, n) * P^*(m, n), \tag{11}$$

where P is the pupil function defined by Eq. (1) and * represents the complex conjugate. For the confocal or two-photon

microscopes, C can be defined as (Wilson and Sheppard, 1984):

$$C_{\text{conf}}(m, n) = C_{\text{conv}}(m, n) * C_{\text{conv}}(m, n). \quad (12)$$

For clarity of explanation, the expressions in this paper are written in terms of continuous integrals and continuous Fourier transforms. In practice, the calculations were performed using sampled functions and discrete Fourier transform algorithms.

Conventional fluorescence microscope

In this section, we describe the effects of aberrations on the imaging properties of conventional non-scanning fluorescence microscopes for different specimen structures. In these microscopes, the two-dimensional (2D) image intensity is described by Eq. (6) which can be rewritten as

$$I(t, w) = \int\int_{-\infty}^{\infty} H_{\text{conv}}(t', w') f(t - t', w - w')\mathrm{d}t'\mathrm{d}w'. \quad (13)$$

Equation (10) can also be written for the conventional fluorescence microscope as

$$I(t, w) = \int\int C_{\text{conv}}(m, n) F(m, n) \exp[-j(tm + wn)]\,\mathrm{d}m\mathrm{d}n. \quad (14)$$

We note that $C_{\text{conv}}(m, n)$ is non-zero only for $\sqrt{m^2 + n^2} < 2$. Either the formulation of Eq. (13) or Eq. (14) can be used to determine the image intensity and the choice depends upon convenience for numerical calculation.

We first model the effects of aberration on the imaging of a point object, for which $f(t, w) = \delta(t)\delta(w)$, where $\delta(.)$ is the Dirac delta function. The on-axis intensity is calculated using Eqs. (13), (7) and (9) as

$$I(0, 0) = H_{\text{conv}}(0, 0) = \left| \int_{r=0}^{1} \int_{\theta=0}^{2\pi} P(r, \theta) r\,\mathrm{d}r\mathrm{d}\theta \right|^2. \quad (15)$$

The second specimen structure that we consider is a line of infinite length oriented along the t-axis. This is described by the specimen function $f(t, w) = \delta(w)$ or alternatively by its Fourier transform $F(m, n) = \delta(m)$. The image of this linear object can be expressed using Eq. (14) as

$$I(t, w) = I(0, w) = \int C_{\text{conv}}(0, n) \exp[-jwn]\,\mathrm{d}n. \quad (16)$$

So the on-axis intensity can be derived as

$$I(0, 0) = \int_{-2}^{2} C_{\text{conv}}(0, n)\mathrm{d}n, \quad (17)$$

where the limits of integration correspond to the finite non-zero extent of the optical transfer function $C_{\text{conv}}(m, n)$. This calculation is performed in the frequency domain, due to the finite support of the integrand.

For a planar object, the specimen function $f(t, w) = 1$, so we find that the on-axis image intensity is given by

$$I(0, 0) = \int\int H_{\text{conv}}(t, w)\mathrm{d}t\mathrm{d}w \quad (18)$$

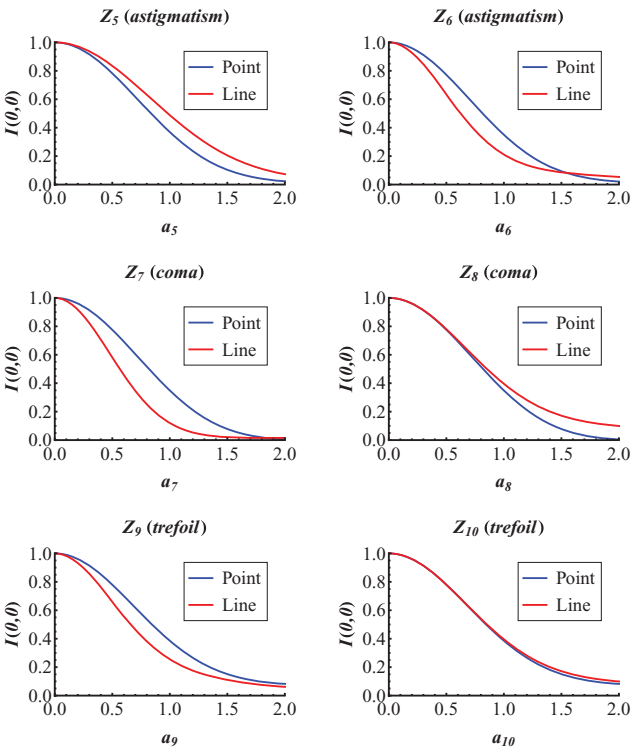

Fig. 1. The on-axis image intensity variation, $I(0,0)$, of point and line structures as a function of single Zernike mode aberration amplitude, a_i, in a conventional fluorescence microscope.

in the spatial domain. More conveniently this can be written as the on-axis image intensity $(t, w = 0)$ in the Fourier domain as

$$I(0, 0) = C_{\text{conv}}(0, 0) = \int\int |P(r, \theta)|^2 r\,\mathrm{d}r\mathrm{d}\theta = const. \quad (19)$$

Because the pupil function varies only in phase and not amplitude, $|P| = 1$. Equation (19) therefore holds for all aberrations and defocus, hence the same constant result is also found for the signal from a uniform volume object. This insensitivity to defocus confirms the well-known phenomenon that the conventional microscope does not exhibit optical sectioning in the manner that the confocal and two-photon microscopes do.

Fig. 1 shows the variation of the on-axis image intensity of the images of point and line specimens, where the specimens lie in the focal plane and individual Zernike aberration modes are present. For each structure, the on-axis intensity is normalized to the value found for zero aberration. In all cases, the peak intensity reduces as aberration amplitude increases. Differences are seen in the relative change in signal level from point and line structures for the different modes. Comparing the graphs for modes 5 and 6 (astigmatism modes that differ only by a 45° rotation), it can be seen that the change in on-axis intensity is identical for the point object, but differs between the two modes for the line object. This is due to the

different relative orientation of the object and the aberration mode, which corresponds to the orientation of the distorted focal spot. Similar effects are seen for mode pairs 7 and 8 (coma) and 9 and 10 (trefoil), which also differ only by rotations.

Confocal and two-photon fluorescence microscopes

In this section, we investigate the effects of aberrations on the imaging of different specimen structures in confocal and two-photon fluorescence microscopes. As with the conventional microscope, the imaging properties of these microscopes can also be described in either the spatial or Fourier domain as shown by Eqs. (6) and (10), respectively.

Expressing Eq. (6) in three dimensions for the confocal case gives

$$I(t, w, 0) = \iiint_{-\infty}^{\infty} H_{\text{conf}}(t', w', u') \times f(t - t', w - w', u')\mathrm{d}t'\mathrm{d}w'\mathrm{d}u'. \quad (20)$$

Equivalently, we can rewrite Eq. (10) using 3D coordinates as

$$I(t, w, 0) = \iiint_{-\infty}^{\infty} C_{\text{conf}}(m, n; u)F(m, n; u) \times \exp[2\pi j(tm + wn)]\mathrm{d}m\mathrm{d}n\mathrm{d}u, \quad (21)$$

where the notation $(m, n; u)$ describes m and n in the frequency domain and u in the spatial domain. Therefore, $F(m, n; u)$ is the 2D Fourier transform of $f(t, w, u)$, transforming (t, w) into (m, n) and not performing any transform in the u direction. We note that $C_{\text{conf}}(m, n; u)$ is the 2D optical transfer function of a confocal microscope taking defocus into account and is non-zero only for $\sqrt{m^2 + n^2} < 4$.

Point, line, plane and volume objects can be described in either the spatial or Fourier domains as shown in Table 1. These definitions are used with Eq. (20) or (21) to give expressions for image intensity for the different specimen structures. We first consider the image of a point object positioned at the origin. For small aberration amplitudes, the maximum intensity of this image is on the optical axis. This on-axis image intensity is given by

$$I(0, 0, 0) = H_{\text{conf}}(0, 0, 0) = \left| \int_{r=0}^{1} \int_{\theta=0}^{2\pi} P(r, \theta) r \mathrm{d}r\mathrm{d}\theta \right|^4 \quad (22)$$

For the line object, the substitution of $f(t, w, u) = \delta(w)\delta(u)$ into Eq. (20) yields

$$I(0, 0, 0) = \int_{-\infty}^{\infty} H_{\text{conf}}(t, 0, 0)\mathrm{d}t. \quad (23)$$

For the planar object, we use Eq. (21) with Eq. (12) and $F(m, n; u) = \delta(m)\delta(n)\delta(u)$ to give the on-axis intensity

$$I(0, 0, 0) = C_{\text{conf}}(0, 0; 0). \quad (24)$$

Equation (24) describes the image signal from a planar object when the plane is located in the focal plane ($u = 0$). When located at an arbitrary position, u, the signal is given by $C_{\text{conf}}(0, 0; u)$. For a volume object we can write the on-axis image intensity as

$$I(0, 0, 0) = \int_u C_{\text{conf}}(0, 0; u)\mathrm{d}u = \iiint_{mnu} |C_{\text{conv}}(m, n; u)|^2 \mathrm{d}m\mathrm{d}n\mathrm{d}u. \quad (25)$$

Table 1. The mathematical description of the 3D specimen structures modelled.

	$f(t, w, u)$	$F(m, n; u)$
Point	$\delta(t)\delta(w)\delta(u)$	$\delta(u)$
Line along t-axis	$\delta(w)\delta(u)$	$\delta(m)\delta(u)$
Plane	$\delta(u)$	$\delta(m)\delta(n)\delta(u)$
Volume	1	$\delta(m)\delta(n)$

Using the expressions derived earlier, we calculated the effects of aberrations on the on-axis image intensity for the different specimen structures in confocal and two-photon microscopes. The on-axis intensity for the four specimen, structures was modelled in the presence of individual Zernike modes for point, line and plane specimens lying in the focal plane. In each case, the aberrated on-axis intensity was normalized to the unaberrated equivalent for the same specimen structure. The results for modes 5–10 are shown in Figure 2.

For all modes and for all structures, as the aberration amplitude increases, the on-axis intensity decreases. As a general trend, it can be seen that the normalized on-axis intensity of the point object is most sensitive to aberrations, followed by the line, plane and volume structures. This confirms the empirical results of Débarre et al. (2009), which showed that the image intensity of a fluorescent bulk should be less sensitive to aberrations than a fluorescent point. As was observed in the results for the conventional microscope, differences can be seen between similar modes (e.g. the astigmatism modes 5 and 6) due to the relative orientation of the linear structure and the aberration mode.

With practical specimens, the induced aberrations generally consist of combinations of aberration modes (Schwertner et al., 2004). The effects of multiple aberration modes on confocal/two-photon imaging of the four structures were also modelled. A set of 100 aberrations consisting of random combinations of Zernike modes 5–30, were derived according to Eq. (3) for a chosen amplitude A. The corresponding on-axis image intensities were calculated for each specimen structure. The mean, 10th and 90th percentiles of the resulting distribution of intensities are plotted in Figure 3. For ease of comparison, the mean values of these distributions are also shown together in Figure 4. The same general trend is seen that the peak intensity from point objects is affected

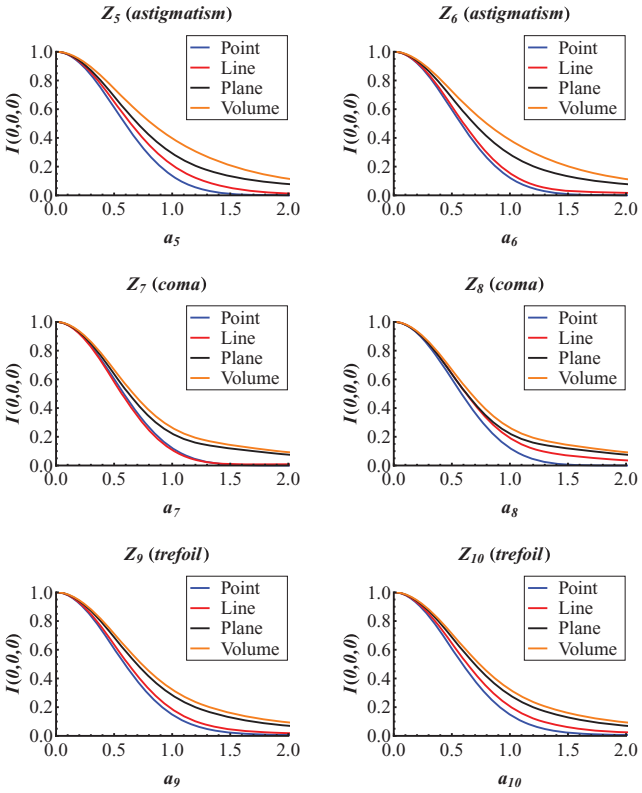

Fig. 2. The on-axis image intensity, $I(0, 0, 0)$, for point, line, plane and volume structures as a function of a single Zernike mode aberration amplitude, a_i in a confocal or two-photon fluorescence microscope.

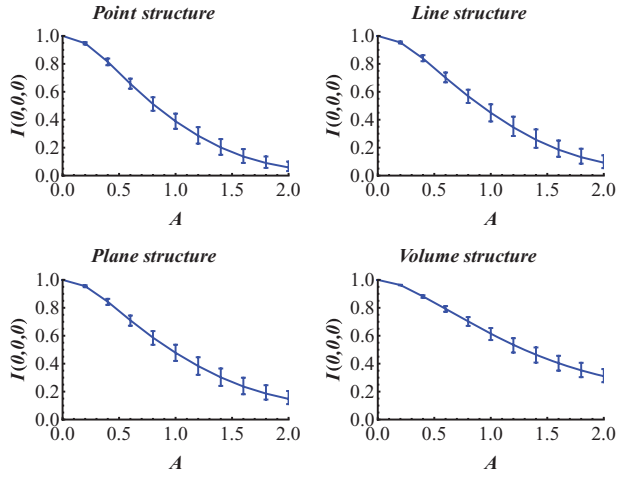

Fig. 3. The mean on-axis image intensity variation, $I(0, 0, 0)$, with aberration amplitude, A, for a point, line, plane and volume structure when imaged in a confocal or two-photon microscope with random combinations of Zernike mode aberrations (modes 5 to 30 were used). The bars mark the 10th and 90th percentiles of the statistical distribution.

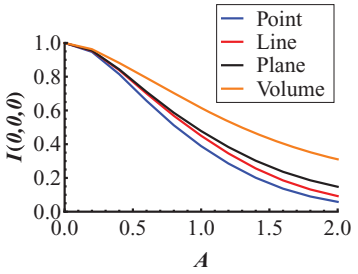

Fig. 4. The mean normalised on-axis intensity variation, $I(0, 0, 0)$ as a function of aberration amplitude, A, for a point (blue), line (red), plane (black) and volume object (orange) when imaged in a confocal or two-photon microscope.

most strongly by aberrations, with linear, planar and volume objects being less affected.

The marked difference between the on-axis intensity detected from the volume object in comparison to the other structures can be explained geometrically. As aberrations are introduced and the effective point-spread function (PSF) increases in size, a significant proportion of the effective PSF will be removed from the region where the point, line and plane objects lie. This in turn reduces the amount of fluorescence detected via the detection PSF and hence leads to a decrease in on-axis image intensity. However, for the volume specimen the distorted focus is always within the fluorescent material and so the on-axis image intensity does not decrease as significantly when compared to the other finer structures.

Comparing Figure 2 with Figure 3, the width of the graphs is noticeably different; the on-axis image intensity variation for a given structure with a random combination of aberrations applied (Fig. 3) has a wider full-width-half-maximum than that for the same structure when individual modes are applied (Fig. 2). This is due to the inclusion of higher order Zernike modes in Fig. 3. Further investigation (not presented here) into the responses to individual higher order modes showed that they give a less significant reduction in intensity at high aberration amplitudes than the lower order modes.

This differential effect of aberrations on the imaging of different specimen structures means that aberrations reduce both the overall image intensity and the relative visibility of objects. Consider, for example, the image of a small fluorescent object superimposed upon a uniform background fluorescence signal. As aberrations become larger the signal from the small object will decrease more rapidly than the signal from the background and, eventually, the small object will become indistinguishable from the background. To quantify this effect, we examine the image contrast when one object is superimposed on another. For example, the image intensity of a fluorescent point object (I_{point}) on a fluorescent plane (I_{plane}) is given by

$$\text{Image intensity} = I_{\text{plane}} + I_{\text{point}} = I_{\text{plane}}\left[1 + \frac{I_{\text{point}}}{I_{\text{plane}}}\right] \quad (26)$$

and so it follows that the contrast of the image of a fluorescent point object embedded in a fluorescent plane is defined as

$$\text{Image contrast} = \frac{I_{\text{point}}(0, 0, 0)}{I_{\text{plane}}(0, 0, 0)}. \qquad (27)$$

Following this definition, the contrast is unity when there is no aberration present and decreases in value as aberration amplitudes increase. Figure 5 shows the contrasts obtained for different combinations of specimen structures and the variation with aberration amplitude. The plots were obtained by calculating the contrast for 100 different random combinations of Zernike mode aberrations (using modes 5–30) and plotting the mean, 10th and 90th percentiles of resulting distribution.

Contrast effects in aberrated microscope images

The results show that the contrast of the point object embedded in a volume object is most strongly affected by aberrations. The general trend is observed that the contrast sensitivity depends upon the relative size (or dimension) of the two specimen structures. For example, for structures embedded in a volume, the sensitivity to aberrations is worst for a point object, followed by the line object then the planar object. Because specimen induced aberrations tend to increase with focal depth, this explains why small objects seem to disappear in a fluorescent (volume-like) background as an image is taken deeper into a sample (see, e.g. Débarre et al., 2008).

We have further simulated the imaging of a combination of idealized specimens, including points, lines and volume objects, in the presence of aberrations. These images are shown in Figure 6. Figure 6(a) shows simulated images of a two-dimensional specimen structure, placed in the focal plane, in which point objects are superimposed upon linear structures. The aberration applied was 0 rad (rms) (left), 1 rad rms (centre) and 2 rad (rms) (right) of Zernike mode 5 (astigmatism). Although the points and lines become less distinct as the aberration increases, the background remains clearly visible. Figure 6(b) shows simulated imaging of a 3D specimen in which an array of point objects lies in the focal plane together with an infinite fluorescent triangular volume object, which extends above and below the focal plane in the bottom right-hand corner of the specimen. For simplicity, the object structure was assumed not to extend outside of the displayed region which has led to the intensity drop-off seen at the edges of Figure 6(b). Figure 6(c) is the cross-sectional on-axis intensity of the images shown in Figure 6(b) along the dashed line, showing clearly the reduction in contrast of the fluorescent points on the background fluorescence as the aberration increases. Figure 2 has previously shown that the on-axis image intensity of a volume-like structure should decrease to approx. 40% of the unaberrated maximum when there is 1 rad. (rms) of Zernike mode 5 and approx. 10% when there is 2 rad. (rms) present, which correlates

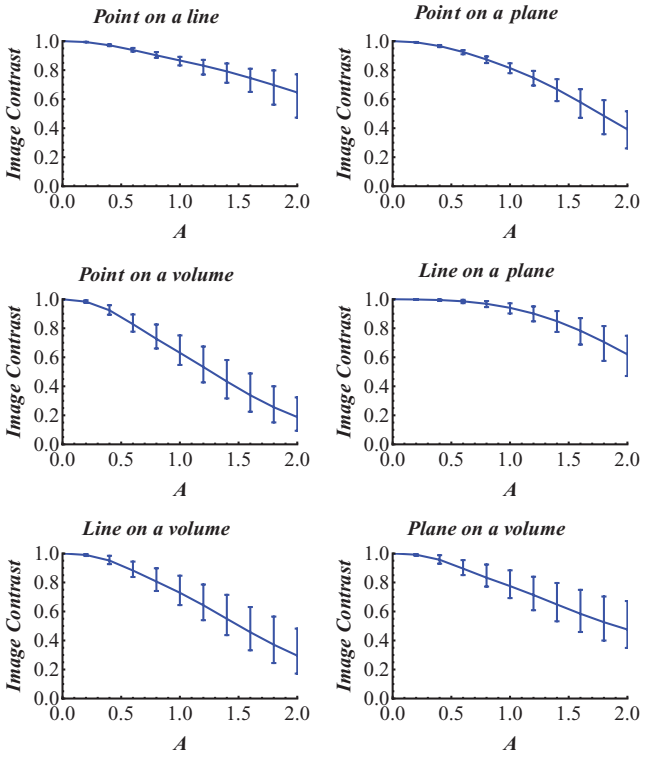

Fig. 5. The variation of confocal or two-photon image contrast as a function of aberration amplitude, *A*, for combinations of specimen structures. The mean, 10th and 90th percentiles of the distribution are shown.

with the background signal reduction shown in Figure 6(c). Significantly, it is the reduction in visibility of the smaller, point-like structures when superimposed on the fluorescent volume-like background that is clear from Figure 6(c), as the relative on-axis intensity drops from approx. 0.1 in the unaberrated case, to approx. 0.03 with 1 rad. (rms) of Zernike mode 5 present and approx. 0.005 with 2 rad. (rms) of Zernike mode 5 present.

Discussion and conclusion

We have shown the variations in effects that aberrations have on conventional, confocal and two-photon fluorescence images for different specimen structures and in particular point-like, linear, planar and volume structures. Although it is well known that aberrations reduce the on-axis intensity of microscope images, we have shown here that they affect the images of different specimen structures to varying extents. The calculations show that the larger the structure is dimensionally, the less sensitive the corresponding on-axis image intensity is to the presence of aberrations. Point-like structures are worst affected, giving the lowest relative on-axis intensity in the presence of aberrations, whereas volume-like structures are the least affected, giving the highest relative on-axis intensity.

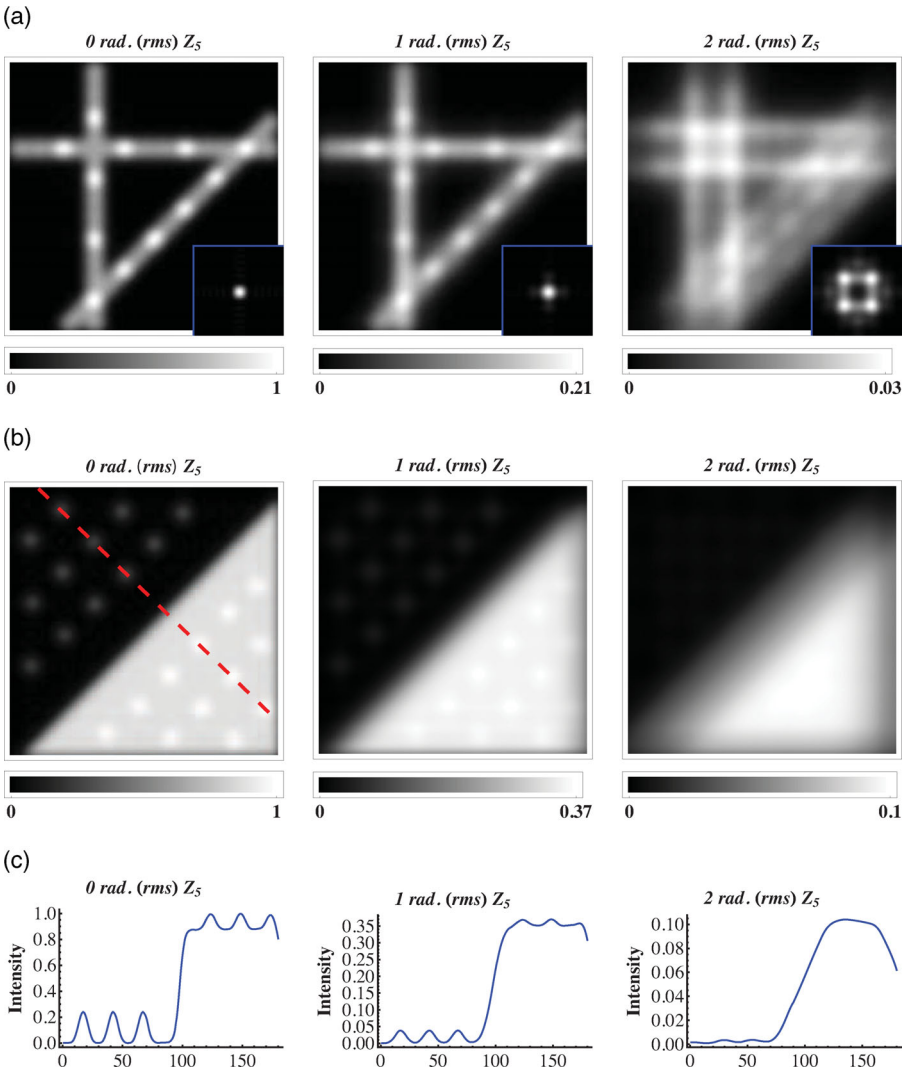

Fig. 6. Images modelling the effect of aberrations, in this case astigmatism (Zernike mode 5), on different structures in a confocal or two photon microscope (a and b), and the cross-sectional on-axis intensity graphs (c), taken from the dashed line in (b). Inset in (a) is the corresponding point-spread function at the same scale as the images. All images in (a) and (b) have been renormalized, as shown by the respective scales.

The contrast between different structures was also shown to be affected by aberrations and the differing contrast causes some fine detail of images to effectively disappear without significant reduction of the background intensity. An important consequence of this phenomenon concerns the effect of aberrations on the visibility of small structures in the presence of larger structures. Such situations frequently occur in biological imaging where fine, low-dimensional features are embedded in a larger, higher-dimensional structure. An example of this would be point-like objects situated within a background volume fluorescence. As the aberration amplitude increases, as might happen for example when focussing deep within a specimen, the volume-like background will retain much more of its brightness than the smaller point-like structures. Eventually, the point-like structures would become effectively invisible as their brightness becomes insignificant compared to the background. This would occur even though an appreciable background would still be visible in the images. This matches experimental observations of the reduction in contrast of small objects in a thick fluorescent specimen (Débarre et al., 2009).

The comparison of the conventional microscope with the confocal or two-photon microscope is emphasized in Figure 7, where we plot the image contrast of a fluorescent point superimposed on a fluorescent plane (both situated in the focal plane) for a conventional and confocal or two-photon microscope. The image contrast is more significantly affected in the case of the conventional microscope than the confocal or two-photon for all modes presented and particularly so at lower aberration amplitudes. This clearly demonstrates

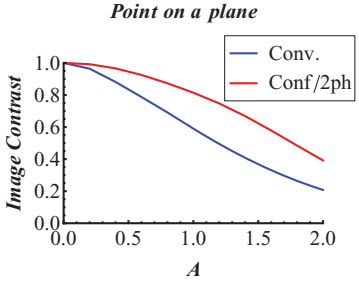

Fig. 7. The variation of image contrast in conventional (Conv.) and confocal or two-photon (Conf/2ph) microscopes as a function of aberration amplitude, *A*, for point specimen structures superimposed on plane specimen structures in the focal plane when aberrated by a random selection of Zernike modes.

the significant advantage of using confocal microscopes over conventional instruments when aberrations are present.

Acknowledgements

This research was supported by funding from the Engineering and Physical Sciences Research Council, UK (grant number EP/E055818/1).

References

Booth, M.J., Neil, M.A.A. & Wilson, T. (1998) Aberration correction for confocal imaging in refractive-index-mismatched media. *J. Microsc.* **192**(2), 90–98.

Booth, M.J. (2007) Wavefront sensorless adaptive optics for large aberrations. *Opt. Lett.* **32**(1), 5–7.

Débarre, D., Botcherby, E.J., Booth, M.J. & Wilson, T. (2008) Adaptive optics for structured illumination microscopy. *Opt. Express* **16**(13), 9290–9305.

Débarre, D., Botcherby, E., Watanabe, T., Srinivas, S., Booth, M. & Wilson, T. (2009) Image-based adaptive optics for two-photon microscopy. *Opt. Lett.* **34**(16), 2495–2497.

Diaspro, A., Federici, F. & Robello, M. (2002) Influence of refractive-index mismatch in high-resolution three-dimensional confocal microscopy. *Appl. Opt.* **41**(4), 685–690.

Gibson, S.F. & Lanni, F. (1992) Experimental test of an analytical model of aberration in an oil-immersion objective lens used in three-dimensional light microscopy. *J. Opt. Soc. Am. A* **9**(1), 154–166.

Girkin, J.M., Poland, S. & Wright, A.J. (2009) Adaptive optics for deeper imaging of biological samples. *Curr. Opin. Biotechnol.* **20**: 106–110.

Gu, M. (1996) *Principles of Three-Dimensional Imaging in Confocal Microscopes*. World Scientific, Singapore.

Hell, S., Reiner, G., Cremer, C. & Stelzer, E.H.K. (1993) Aberrations in confocal fluorescence microscopy induced by mismatches in refractive index. *J. Microsc.* **169**(3), 391–405.

Ji, N., Milkie, D.E. & Betzig, E. (2010) Adaptive optics via pupil segmentation for high-resolution imaging in biological tissues. *Nat. Methods* **7**(2), 141–147.

Mahajan, V.N. (1994) Zernike circle polynomials and optical aberrations of systems with circular pupils. *Supplement to Applied Optics*, **33**(34), 8121–8124.

Schwertner, M., Booth, M.J., Neil, M.A.A. & Wilson, T. (2004) Measurement of specimen-induced aberrations of biological samples using phase stepping interferometry. *J. Microsc.* **213**(1), 11–19.

Schwertner, M., Booth, M.J. & Wilson, T. (2007) Specimen-induced distortions in light microscopy. *J. Microsc.* **228**(1), 97–102.

Tango, W.J. (1977) The circle polynomials of zernike and their application in optics. *Appl. Phys.* **13**, 327–332.

Wilson, T. & Sheppard, C. (1984) *Theory and Practice of Scanning Optical Microscopy*. Academic Press, London.

Appendix: Zernike polynomials

The phase aberration can be expressed as a Zernike series (Tango, 1977):

$$\phi(r,\theta) = \sum a_n^m Z_n^m(r,\theta), \tag{28}$$

where a_n^m is the amplitude of mode m, n and Z_n^m is the Zernike polynomial. Zernike polynomials are orthonormal functions over the unit circle and are most readily expressed in polar coordinates as

$$Z_n^m(r,\theta) = \begin{cases} m < 0 & \sqrt{2}\mathcal{R}_n^{-m}(r)\sin(-m\theta), \\ m = 0 & \mathcal{R}_n^0(r), \\ m > 0 & \sqrt{2}\mathcal{R}_n^m(r)\cos(m\theta), \end{cases} \tag{29}$$

where $\mathcal{R}_n^m(r)$ is defined as

$$\mathcal{R}_n^m(r) = \sqrt{n+1} \sum_{s=0}^{(n-m)/2} \frac{(-1)^s (n-s)!}{s!\left(\frac{n+m}{2}-s\right)!\left(\frac{n-m}{2}-s\right)!} r^{n-2s}. \tag{30}$$

The order n of the polynomial may be any positive integer or 0 but the index m is restricted to n, $\pm(n-2)$, ..., 0 (Table 2). It is useful to be able to refer to the various modes by using a single index. The index i is commonly used, starting at 1 and increasing in integer steps for rising n then with rising magnitude of m, as shown in Table 2 (Mahajan, 1994).

The mean of $Z_n^m(r,\theta)$ over the unit circle is zero, provided $n \neq 0$ (when $n = 0$ the mean value is 1 rad. rms). The polynomials form a complete function basis so can be combined to produced any phase aberration desired.

Table 2. The first 30 Zernike polynomials.

i	n	m	$Z_i(r,\theta)$	Aberration term
1	0	0	1	piston
2	1	1	$2r\cos(\theta)$	tip
3	1	−1	$2r\sin(\theta)$	tilt
4	2	0	$\sqrt{3}(2r^2-1)$	defocus
5	2	2	$2\sqrt{3}r^2\cos(2\theta)$	astigmatism
6	2	−2	$2\sqrt{3}r^2\sin(2\theta)$	astigmatism
7	3	1	$2\sqrt{2}(3r^3-2r)\cos(\theta)$	coma
8	3	−1	$2\sqrt{2}(3r^3-2r)\sin(\theta)$	coma
9	3	3	$2\sqrt{2}r^3\cos(3\theta)$	trefoil
10	3	−3	$2\sqrt{2}r^3\sin(3\theta)$	trefoil
11	4	0	$\sqrt{5}(6r^4-6r^2+1)$	spherical
12	4	2	$\sqrt{10}(4r^4-3r^2)\cos(2\theta)$	astigmatism (2nd order)
13	4	−2	$\sqrt{10}(4r^4-3r^2)\sin(2\theta)$	astigmatism (2nd order)
14	4	4	$\sqrt{10}r^4\cos(4\theta)$	tetrafoil
15	4	−4	$\sqrt{10}r^4\sin(4\theta)$	tetrafoil
16	5	1	$2\sqrt{3}(10r^5-12r^3+3r)\cos(\theta)$	coma (2nd order)
17	5	−1	$2\sqrt{3}(10r^5-12r^3+3r)\sin(\theta)$	coma (2nd order)
18	5	3	$2\sqrt{3}(5r^5-4r^3)\cos(3\theta)$	trefoil (2nd order)
19	5	−3	$2\sqrt{3}(5r^5-4r^3)\sin(3\theta)$	trefoil (2nd order)
20	5	5	$2\sqrt{3}r^5\cos(5\theta)$	pentafoil
21	5	−5	$2\sqrt{3}r^5\cos(5\theta)$	pentafoil
22	6	0	$\sqrt{7}(20r^6-30r^4+12r^2-1)$	spherical (2nd order)
23	6	2	$\sqrt{14}(15r^6-20r^4+6r^2)\cos(2\theta)$	astigmatism (3rd order)
24	6	−2	$\sqrt{14}(15r^6-20r^4+6r^2)\sin(2\theta)$	astigmatism (3rd order)
25	6	4	$\sqrt{14}(6r^6-5r^4)\cos(4\theta)$	tetrafoil (2nd order)
26	6	−4	$\sqrt{14}(6r^6-5r^4)\sin(4\theta)$	tetrafoil (2nd order)
27	6	6	$\sqrt{14}(r^6)\cos(6\theta)$	hexafoil
28	6	−6	$\sqrt{14}(r^6)\sin(6\theta)$	hexafoil
29	7	1	$4(35r^7-60r^6+30r^3-4r)\cos(\theta)$	coma (3rd order)
30	7	−1	$4(35r^7-60r^6+30r^3-4r)\sin(\theta)$	coma (3rd order)